

Journal of Biomedical Optics

SPIEDigitalLibrary.org/jbo

Automated segmentation of multiple red blood cells with digital holographic microscopy

Faliu Yi
Inkyu Moon
Bahram Javidi
Daniel Boss
Pierre Marquet

Automated segmentation of multiple red blood cells with digital holographic microscopy

Faliu Yi,^a Inkyu Moon,^a Bahram Javidi,^b Daniel Boss,^c and Pierre Marquet^{c,d}

^aChosun University, School of Computer Engineering, 375 Seosuk-dong, Dong-gu, Gwangju, 501-759 Republic of Korea

^bUniversity of Connecticut, Department of Electrical and Computer Engineering U-2157, Storrs, Connecticut 06269-2157

^cLNDC, BMI, Ecole Polytechnique Fédérale de Lausanne, Lausanne, Switzerland

^dDépartement de Psychiatrie DPCHUV, Centre de Neurosciences Psychiatriques, PrillyLausanne, Switzerland

Abstract. We present a method to automatically segment red blood cells (RBCs) visualized by digital holographic microscopy (DHM), which is based on the marker-controlled watershed algorithm. Quantitative phase images of RBCs can be obtained by using off-axis DHM along to provide some important information about each RBC, including size, shape, volume, hemoglobin content, etc. The most important process of segmentation based on marker-controlled watershed is to perform an accurate localization of internal and external markers. Here, we first obtain the binary image via Otsu algorithm. Then, we apply morphological operations to the binary image to get the internal markers. We then apply the distance transform algorithm combined with the watershed algorithm to generate external markers based on internal markers. Finally, combining the internal and external markers, we modify the original gradient image and apply the watershed algorithm. By appropriately identifying the internal and external markers, the problems of oversegmentation and undersegmentation are avoided. Furthermore, the internal and external parts of the RBCs phase image can also be segmented by using the marker-controlled watershed combined with our method, which can identify the internal and external markers appropriately. Our experimental results show that the proposed method achieves good performance in terms of segmenting RBCs and could thus be helpful when combined with an automated classification of RBCs. © 2013 Society of Photo-Optical Instrumentation Engineers (SPIE) [DOI: 10.1117/JBO.18.2.026006]

Keywords: three-dimensional image processing; red blood cells analysis; red blood cells phase image segmentation; digital holographic microscopy; medical and biological imaging; watershed segmentation.

Paper 12501 received Aug. 7, 2012; revised manuscript received Dec. 25, 2012; accepted for publication Jan. 4, 2013; published online Feb. 1, 2013.

1 Introduction

Three-dimensional (3-D) computational imaging techniques have received increased attention with advances in 3-D digital holographic imaging systems.¹⁻¹⁰ Three-dimensional image-processing of holographic images have been suggested for the segmentation, recognition, and tracking of macro or micro objects.¹¹⁻¹⁶ However, because of the unnecessary background noise in the computational holographic image, it is necessary to perform holographic image segmentation.¹⁶ Since most image segmentation methods are time-consuming and not very accurate, the need for automated accurate holographic image segmentation is imperative.

Analysis of the red blood cell (RBC) morphological characteristics in the peripheral blood is an important step to assess hematological functions and the presence of disease. However, the remarkable morphology variation of RBC represents a significant challenge for an automated analyzer. Consequently, an important proportion of RBC samples still require a time-consuming manual examination. Within this framework, we have developed an original automated segmentation algorithm specifically dedicated to process DHM quantitative phase images, presenting the advantage to provide relevant quantitative cell parameters including cell size, shape and volume, as well as mean corpuscular hemoglobin (MCH) and MCH

concentration for RBCs.¹⁷ Furthermore, the segmented quantitative phase images of RBCs also benefit the tracking of single or multiple RBCs for their dynamics (3-D morphology and biomass changes) analysis.

Since the quantitative phase images allow the identification of the internal and external regions for a single RBC, it is better to separate those different regions, respectively, in order to comprehensively analyze RBCs in detail. Thus, segmenting the inside and outside RBC regions is also significant. Segmentation approaches can be classified into two categories.^{18,19} One is based on the intensity value and the other is related to the edge of objects. Some of the regions in the single RBC have phase values very close to the background value. This is shown in Fig. 1(a). Consequently, it is not easy to obtain accurate quantitative phase image segmentation with only an intensity based method like threshold algorithms. The other problem is that most single RBCs, due to their discoid shape, have two gradients. One gradient is between an RBC and the background, while the other lies inside the single RBC surface, as shown in Fig. 1(b) and 1(c). This makes it difficult to segment the RBC cells with an algorithm based only on edge-detection. Due to the gradient within the RBC, inaccurate segmentation is always generated. Furthermore, some of the RBCs are connected to each other, as shown in Fig. 1(d). This can also affect the segmentation of isolated RBC. All of these problems complicate the quantitative phase images segmentation of RBCs.

Address all correspondence to: Inkyu Moon, Chosun University, School of Computer Engineering, 375 Seosuk-dong, Dong-gu, Gwangju. 501-759 Republic of Korea. Tel: 82622306033; E-mail: inkyu.moon@chosun.ac.kr

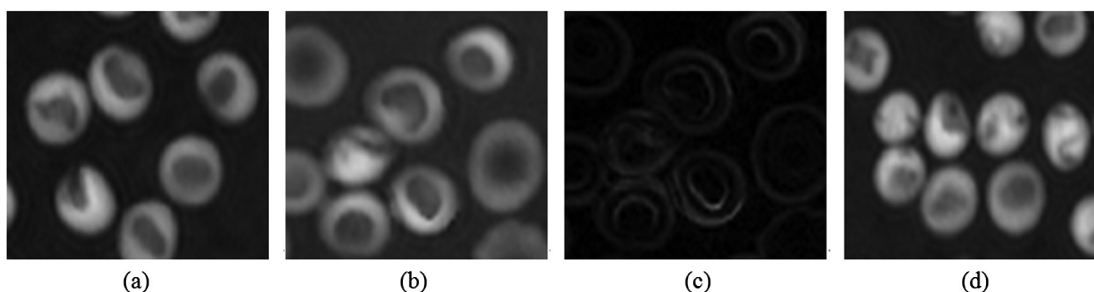


Fig. 1 Some characteristics of red blood cells quantitative phase image. (a) Some regions in the single RBC have phase values similar to the background value, (b) the original RBCs quantitative phase image with two kinds of edges (inside and outside parts), (c) the gradient image of (b), and (d) some of the RBCs connected to each other.

In a recent paper,²⁰ we demonstrated that it was possible to extract feature patterns to discriminate between RBC populations that differ in shape and hemoglobin using RBC quantitative phase images obtained with off-axis digital holographic microscopy (DHM).^{21,22} In this paper, we present a detailed explanation of the automatic method to segment the RBC quantitative phase image for the purpose of accurate calculation of the RBC phase value and show that the proposed segmentation method efficiently reduces over- and under-segmentation. Specifically, our automated RBC segmentation algorithm can be suitable for the quantitative comparison of different types of RBCs since the phase values in the background parts of the RBCs quantitative phase image can be set to zero value. First, an Otsu algorithm is applied to obtain the binary image, then, a morphology operation is conducted on the binary image. After a series of morphology operations, such as morphological opening, erosion and reconstruction, we can get the proper internal markers of these cells, which can avoid the effect of internal gradient and connection among different cells. With the internal markers, we generate the external markers by using the distance transform algorithm combined with the watershed algorithm.¹⁹ Finally, we apply the watershed algorithm to the modified gradient image obtained by the minima imposition technique²³ with the extracted internal and external markers. With these methods, good experimental results are presented.

This paper is organized as follows. Sections 2 and 3 briefly describe the off-axis holographic microscopy and the marker-

controlled watershed algorithm. In Sec. 4, the procedure of the proposed method for RBC segmentation is presented. Then, the performance evaluation method and experimental results are given in Sec. 5. Finally, we conclude this paper in Sec. 6

2 Sensing and Imaging of RBCs by Using Off-Axis DHM

Figure 2 shows a schematic of the off-axis digital holographic microscopy for 3-D sensing and imaging of RBCs used in the experiments. In this optical setup, the coherent beam coming from the laser with a wavelength of 682 nm is divided into reference and object beams. A $40\times/0.75$ NA microscope objective magnify the object beam diffracted by the RBC specimen. The magnified object beam interferes with the reference beam in the off-axis geometry. The CCD camera records the off-axis digital hologram of RBCs. From the recorded digital hologram, the RBC 3-D imaging is achieved by using the numerical algorithms.^{21,22}

3 Marker-Controlled Watershed Algorithm

The watershed transform algorithm is particularly suitable for generating a closed boundary of the objects in question.²⁴ It also shows good performance, but it may often result in over-segmentation. To address this problem, a standard watershed transform algorithm has been enhanced with marker control. In this section we will discuss both algorithms.

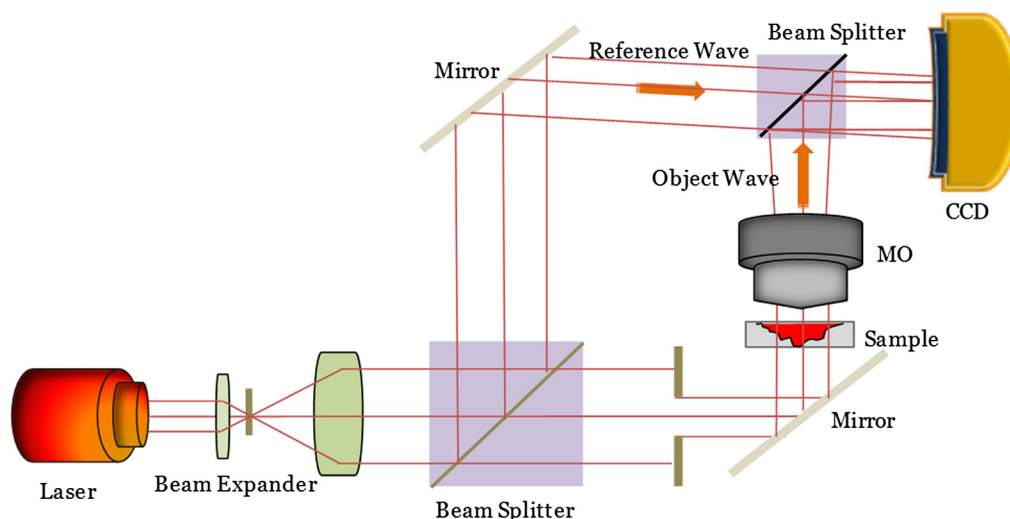


Fig. 2 Schematic of the off-axis digital holographic microscopy used in the experiments.

3.1 Watershed Transform Algorithm

The watershed transform algorithm is based on flooding simulation. We consider intensity values as terrain elevations, where regional minimal values are regarded as valleys and regional maximal values as the peaks. When water floods the terrain, dams are built among different valleys. The watershed transform algorithm finds the peak value between the two valleys as shown in Fig. 3. These peaks form the watershed line.

Let us see how this is implemented using Meyer's algorithm.²⁵ First, a set of markers is selected as "valleys" and is assigned different labels. Then, all neighboring pixels of each labeled area are added to the priority queue with a priority level, which depends on the label's intensity value. After that, the label with the highest priority is picked from the priority queue. If the neighbors of the selected value, which are already labeled, have the same label, these neighboring values are labeled the same. At that, all nonlabeled neighbors are added to the priority queue. This step is repeated until the priority queue is empty. Finally, nonlabeled intensity values are the peak values (see Fig. 3) that are included in the watershed lines.

3.2 Marker-Controlled Watershed

In the watershed transform algorithm, water floods the terrain starting from the regional minimal value. This goes, however, according to the markers and the maximum values between every two markers are calculated. These maximal values are the watershed lines. The marker-controlled watershed algorithm further distinguishes between internal and external markers. Internal markers represent objects that we are looking for. So, in order to get correct objects, we should mark all objects as internal markers. Usually, internal markers are obtained with a threshold algorithm. On the other hand, external markers represent the background around the objects. A better way to obtain external markers is the distance transform algorithm combined with the watershed algorithm with internal markers. Distance transform is the distance from every pixel to the nearest non-zero-valued pixel.¹⁹

Usually, the watershed transform is applied to gradient images because the objects and the background both have low values, while edges correspond to high values in the gradient image. Unfortunately, due to noise and other local irregularities of the gradient image, it always contains a large number of regional minimal values. Accordingly, the segmentation result is not good enough. In marker-controlled watershed, after internal and external markers are obtained, they are used to modify the gradient image. Using the minimal imposition technique,²³ only positions where marker values are located become regional minima. Thus, unnecessary regional minimal

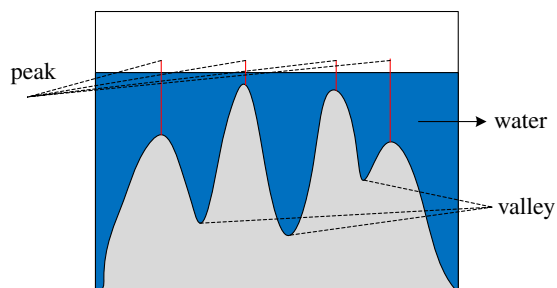


Fig. 3 Flooding simulation model of the watershed algorithm.

values can be efficiently removed and we can apply the watershed transform algorithm to the modified gradient image. An example of such processing is shown in Fig. 4.

4 Segmentation Based on Marker-Controlled Watershed

Although the existing marker-controlled watershed method described in Ref. 19 provides a better way to reduce oversegmentation, it cannot efficiently extract internal and external markers. Thus, we present a method for efficient extraction of markers in the quantitative phase image of RBCs based on the enhanced marker-controlled watershed algorithm. By using this method, we can solve problems shown in Fig. 1. Furthermore, undersegmentation can be avoided. The steps of the enhanced marker-controlled watershed for RBCs quantitative phase image segmentation are as follows:

- Step 1: Normalize RBC phase image. Denote as I_{nom} .
- Step 2: Segment I_{nom} using Otsu's method²⁶ and fill the holes using morphological reconstruction.¹⁹ Denote as I_{bin} . The Otsu's method can be represented as following:

$$\sigma^2(t) = \omega_1(t)\omega_2(t)[\mu_1(t) - \mu_2(t)]^2, \quad (1)$$

where $\sigma^2(t)$ is the variance of the inter-class, $\omega_i(t)$ and $\mu_i(t)$ are the class probability and class means, respectively. The variable t , which can maximize the inter-class variance $\sigma^2(t)$, is the required threshold.

- Step 3: Obtain the gradient magnitude of the original phase image. Denote as I_{grad} . Here, Sobel operator was used to calculate the gradient in both vertical and horizontal directions:

$$g_x = \begin{bmatrix} -1 & 0 & 1 \\ -2 & 0 & 2 \\ -1 & 0 & 1 \end{bmatrix} * I_{bin} \quad \text{and} \quad g_y = \begin{bmatrix} -1 & -2 & -1 \\ 0 & 0 & 0 \\ 1 & 2 & 1 \end{bmatrix} * I_{bin} \quad (2)$$

$$I_{grad} = \sqrt{(g_x^2 + g_y^2)} \quad (3)$$

where I_{grad} is the image of gradient magnitude, I_{bin} and $*$ are source image and the symbol of convolution operation, respectively.

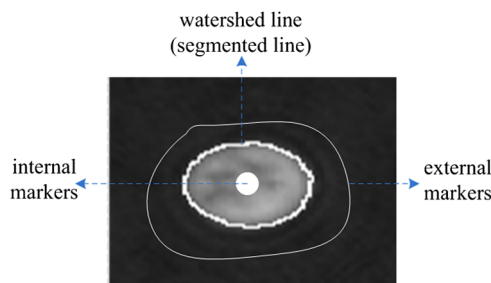


Fig. 4 An example of experimental results for marker-controlled watershed algorithm.

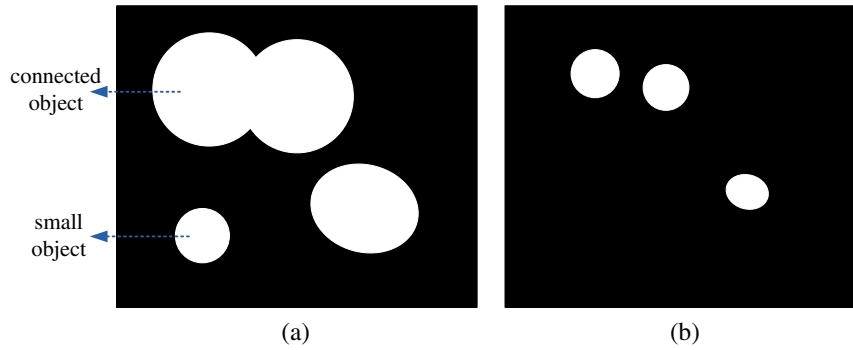


Fig. 5 (a) Connected and small objects (b) erosion of the image in (a) where disk structuring element is so large that small objects are lost.

Step 4: Obtain internal markers.

- Apply morphological opening¹⁹ to I_{bin} with disk-structuring element of radius 9 denoted as I_{open1} . Such an element is much smaller than the smallest RBC, so all required objects will be preserved while additional noise is removed.
- Apply morphological erosion to I_{open1} with disk-structuring element of radius 17. Get image I_{ero1} . Such an element is about medium size of RBC. As a result, connected objects will be separated.
- Take image I_{ero1} as a marker and image I_{open1} as a mask, and apply the morphological reconstruction operation to them. Denote the obtained image as I_{rec1} .
- Subtract I_{rec1} from I_{open1} . Denote the obtained image as I_{sma1} . When separation of the connected cells is necessary, as shown in Fig. 5(a), use a disk-structuring element with radius 17 as described in Step 4a to erode the image. This can, however, totally erode small RBCs as shown in Fig. 5(b). If no precautions are taken, this will result in under-segmentation; small RBCs will be lost. So, the purpose of this step is to get back small-size cells.
- Apply the morphological dilation to image I_{ero1} with disk-structuring element of radius 11. This step reduces the effect of internal gradients as described in Fig. 1(b), as it extends the center area so that it now covers the internal gradient. Denote as I_{dila} .
- Combine the image I_{sma1} (Step 4d) with the image I_{dila} (Step 4e) The result, which has marked most of the objects, can be used as internal markers. Denote as I_{inter} .

Step 5: Obtain external markers from image I_{inter} (Step 4e) using the distance transform algorithm and watershed transform. Denote as I_{exter} . To calculate the distance from each pixel to the nearest nonzero-value pixel, use the equation below:

$$\begin{cases} D(x_i, y_i) = 0 & \text{if } O(x_i, y_i) = 1 \\ D(x_i, y_i) = \sqrt{[(x_i - x_j)^2 + (y_i - y_j)^2]} & \text{if } O(x_i, y_i) = 0 \end{cases} \quad (4)$$

where $D(x, y)$ is the distance transform image, $O(x, y)$ is the source image and $O(x_j, y_j)$ is the nearest nonzero value pixel of $O(x_i, y_i)$.

Step 6: Combine internal markers from I_{inter} with external markers from I_{exter} , and get final markers image I_{mark} . Now, we can modify the gradient magnitude image I_{grad} obtained in Step 3 by using the minimal imposition technique²³ as follows (see Ref. 27):

$$I_{modify} = R_{(I_{grad}+1) \wedge I_{mark}}^e(I_{mark}), \quad (5)$$

where $R_{(I_{grad}+1) \wedge I_{mark}}^e(I_{mark})$ is the morphological erosion reconstruction of I_{mark} from $(I_{grad} + 1) \wedge I_{mark}$, and symbol \wedge stands for the point-wise minimum between $(I_{grad} + 1)$ and I_{mark} . Finally, the watershed transform algorithm is applied to the modified gradient image I_{modify} , and we get a reasonably segmented phase image I_{obj} .

Figure 6 is the flow chart of the proposed method. In this enhanced marker-controlled watershed, we can efficiently and correctly extract internal and external markers. It also has the advantage of reducing problems with both over- and under-segmentation.

After obtaining the segmented RBCs, we move to segmenting the inner and the outer parts of the RBC based on the segmented phase image I_{obj} . The segmentation procedure can be described as follows:

Step 1: Get the gradient image (using Sobel operation on both vertical and horizontal directions) and binary mask image of I_{obj} . Denote these as I_{grad2} and I_{bin} , respectively.

Step 2: Obtain external markers.

Erode the binary mask image I_{bin} using disk structuring elements of radiuses 5 and 7, respectively. Get images I_{erod1} and I_{erod2} . Then apply the complement operation to I_{erod1} and I_{erod2} , denote the obtained images as I_{comp1} and I_{comp2} . The image I_{comp1} is the needed external markers, denote as I_{exter2} .

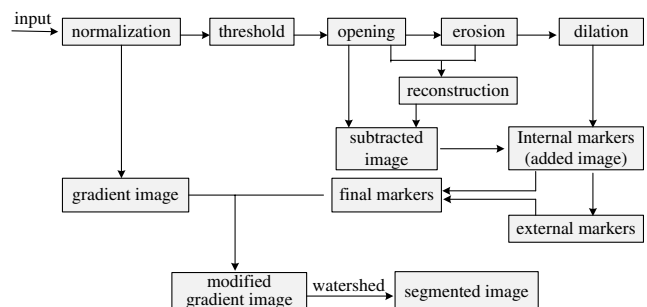


Fig. 6 Flowchart of the proposed phase image segmentation method.

Step 3: Obtain internal markers.

- a. Multiply I_{obj} by I_{erod2} , add the resulting image with I_{comp2} , and get image I_{add} .
- b. Segment I_{add} using the threshold method (set threshold to 0.45). Denote the segmented image as I_{thre1} .
- c. Obtain internal markers I_{inter2} by applying morphological close to the complemented image I_{thre1} with a disk-structuring element of radius 5.

Step 4: Get new markers I_{mark2} by combining internal markers from I_{inter2} and external markers from I_{exter2} .

Step 5: Modify the gradient phase image I_{grad2} with I_{mark2} using the minimal imposition technique. Get image $I_{modify2}$.

Step 6: Obtain the inner part of the RBC image I_{inside} by applying the watershed algorithm to $I_{modify2}$.

Step 7: Obtain the outer part of RBCs image $I_{outside}$ by subtracting I_{inside} from I_{obj} .

5 Performance Evaluation

5.1 Performance Evaluation Method

In this subsection, we have applied a scientific tool developed by F. Sadjadi,²⁸ which is based on the experimental design methodology and independent of the system's output, for performance evaluation. The performance comparison of two algorithms with biased results is mainly dependent on the varied parameters in segmentation. The procedure of the performance evaluation approach can be briefly described as steps of data characterization, data sampling, primary parameter selection, parameter sampling, performance metrics definition, performance model calculation and statistical analysis. The quantitative phases of RBCs in this study are numerically reconstructed from their digital hologram, which is recorded by using off-axis digital holography microscopy (see Fig. 2) and the RBC quantitative phase images (QPIs) are given to two categories, namely newer (with a 14-day storage period) and older (with a 38-day storage period) RBC QPIs. The primary parameter that largely affects the segmentation result in our procedure is the value of threshold obtained by Otsu's method in Step 2 of Sec. 4 while the main parameter for the marker-controlled watershed in Ref. 19 is also a threshold used to find the regional minimum values. We will not analyze the performance evaluation of the watershed algorithm since there are no parameter in it and the result is intuitively unsatisfactory [see Fig. 7(c) and 7(d)]. Also, the assessment of segmentation results for RBC inner and outer parts are not conducted because they rely heavily on the previous segmentation results. For the performance metrics, the segmentation accuracy is adopted and it is simply defined as the absolute value of correlation between segmented RBCs image and reference image, which is manually obtained. The closer the segmented image is to the reference image, the closer the segmentation accuracy will tend to approach 1. Consequently, the analyzed data consist of newer and older RBC QPIs, while the range of the parameters and segmentation accuracy is defined between 0 and 1. Accordingly, 21 sample data were extracted from the parameters range and tested in order to form performance model for each method. The threshold used in Ref. 19 was sampled by interval of 0.05 and then the segmentation accuracy was computed correspondingly. Similarly, the threshold values in our proposed segmentation

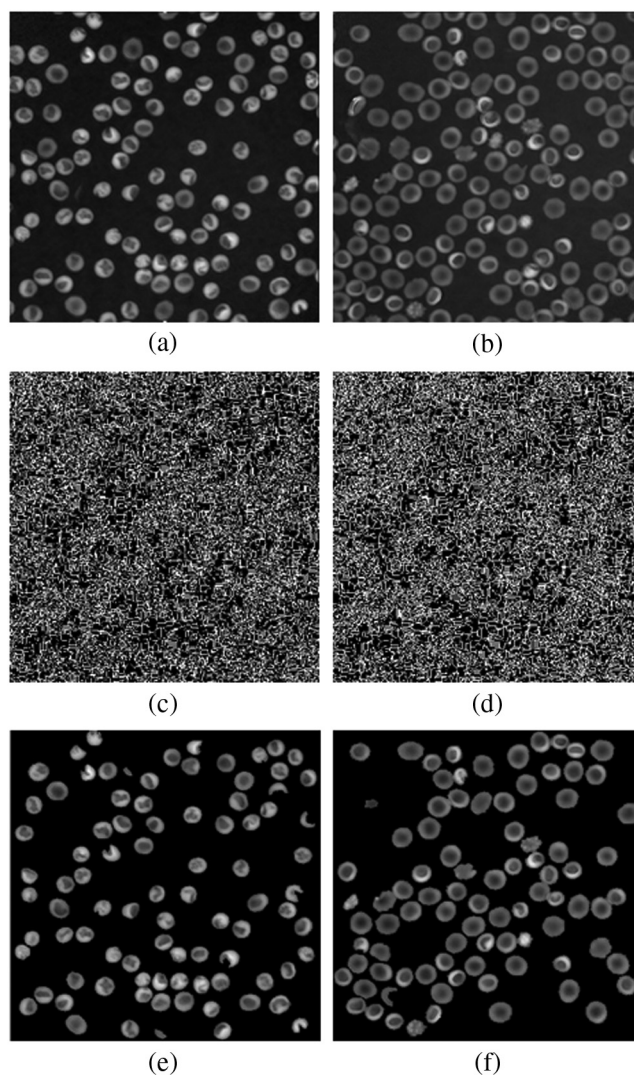


Fig. 7 RBC phase images. (a) Newer RBCs. (b) Older RBCs. (c) and (d) are the corresponding segmentation results using standard watershed algorithm. (e) and (f) Are the results using the marker-controlled watershed algorithm.

method also vary from 0 to 1 with an interval of 0.05. For curve-fitting, the least square error estimation technique^{28,29} was employed and the polynomials were examined with degrees up to 6. Then, statistical analysis of Chi-squared test was performed for checking of the similarity between the obtained results (the measured data with the segmentation method and that in the fitted polynomial).^{29,30}

5.2 Experimental Results

As the method presented in Sec. 5.1, the performance model of segmentation scheme in Ref. 19 was conducted between segmentation accuracy and varied threshold, as shown in Fig. 8(a) and 8(b) for new and old RBC QPIs, respectively. The homologous performance models between segmentation accuracy and threshold for newer and older RBC QPIs in our proposed approach are presented in Fig. 8(c) and 8(d). Consequently, the p -values in Chi-squared test for the null hypothesis that the predictive performance models approximately satisfy with the measured response curve were achieved

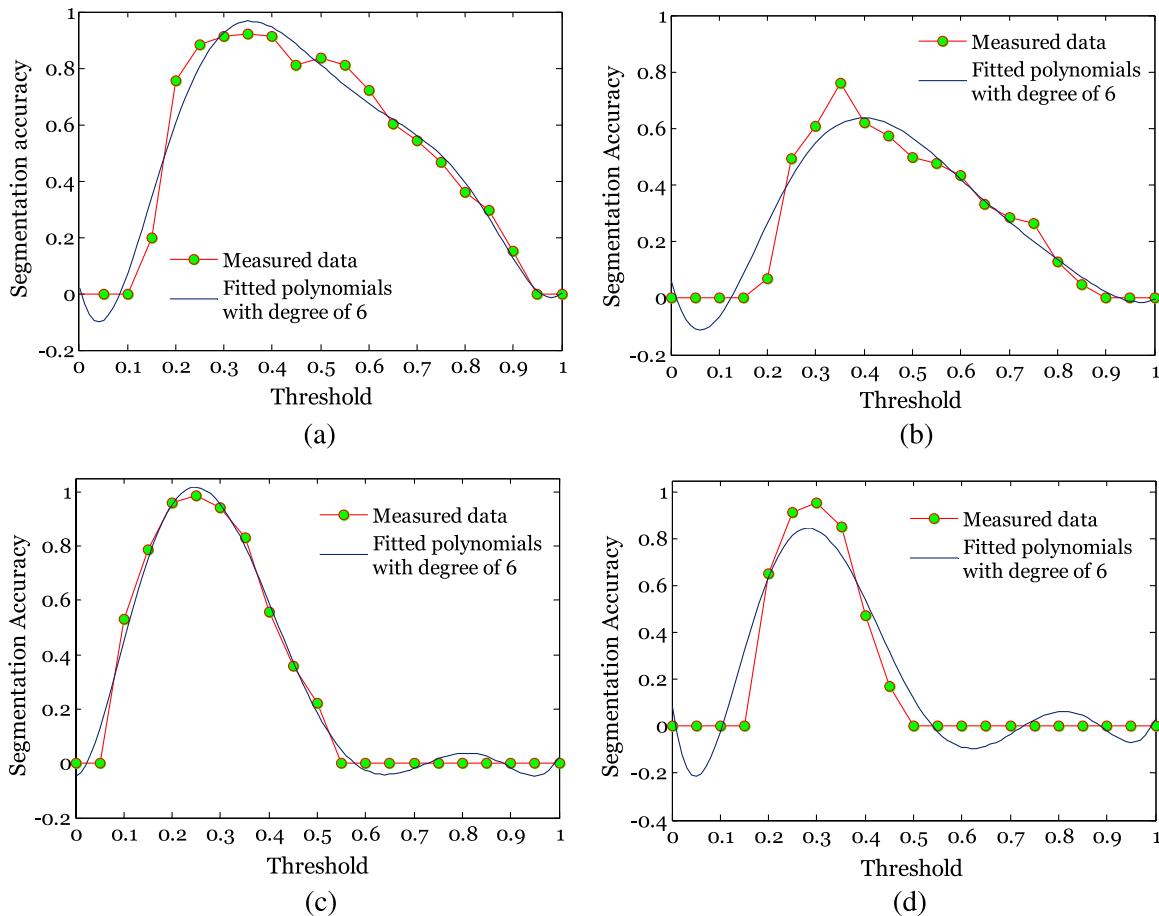


Fig. 8 Performance models. (a) and (b) Are performance models for newer and older RBC QPIs in the method of Ref. 19. (c) and (d) Are performance models for newer and older RBC QPIs in our proposed procedure.

to be 0.7578, 0.3571, 0.9135, and 0.1213 for Fig. 8(a)–8(d), respectively. Therefore, the null hypothesis that the fitting curve is similar to the measured one should be accepted at the 0.05 level of significance. It is also noted that some values of segmentation accuracy in the fitted curve go below 0 or above 1, which are beyond the range of segmentation accuracy. This is because the curve approximately fits the measured data.

It is noted that the maximum segmentation accuracy in our method outperforms that presented in Ref. 19 and the appropriate threshold is approximated to be 0.27 and 0.30 for newer and older RBC QPIs, respectively, which is similar with the values obtained by Otsu’s method used in Step 2 for newer and older RBC QPIs. Thus, it proves that the Otsu’s method can be used for automatically finding the threshold that can reduce the uncertainty of segmentation results by setting a random value.

Next, the segmentation results of RBC QPIs with varied methods using the found appropriate parameters are presented for intuitional observation. Furthermore, segmentation results about inner and outer parts of the RBC QPIs are also shown. Here, we still use two classes of RBCs corresponding to two different durations of storage to illustrate the robustness of our method (more than 100 images are tested). Indeed, it has been suggested that during storage, preserved blood cells undergo progressive structural and functional changes that may reduce red-cell function and viability after transfusion.³¹ The first class is newer RBCs with a 14-day storage period, while the second is older RBCs with a 38-day storage period.

Figure 7 shows the respective segmented images using the classical watershed and the marker-controlled watershed described in Ref. 19.

From Fig. 7 one can see that without further processing, both the standard and the marker-controlled watershed methods cannot yield accurate enough segmentation results, as they cannot properly handle over- and undersegmentation problems. Figure 9 shows experimental results obtained with the enhanced marker-controlled watershed. One can see that both internal and external markers are properly extracted.

Using the proposed enhanced marker-controlled watershed algorithm, we obtained good experimental results for segmentation of the RBC QPIs. The algorithm is reasonably efficient in reducing both over- and under-segmentation, as well as properly separating the cells that touch one another. After successfully segmenting the RBC QPIs using the method described in Sec. 4, we can also accurately obtain the internal and external parts of the holographic QPIs of RBCs, respectively, by using proposed method. Figure 10 shows the segmentation result of the inner and outer parts of the RBCs images from Fig. 9(a) and 9(b).

After segmentation, the background phase value of all QPIs can be set to zero. Then, the average phase in the background region can be used to determine the average phase within a single RBC so that it is possible for one to directly compare QPIs with each other, such as the QPIs of the two different RBC classes. On the other hand, the achieved average phase in the

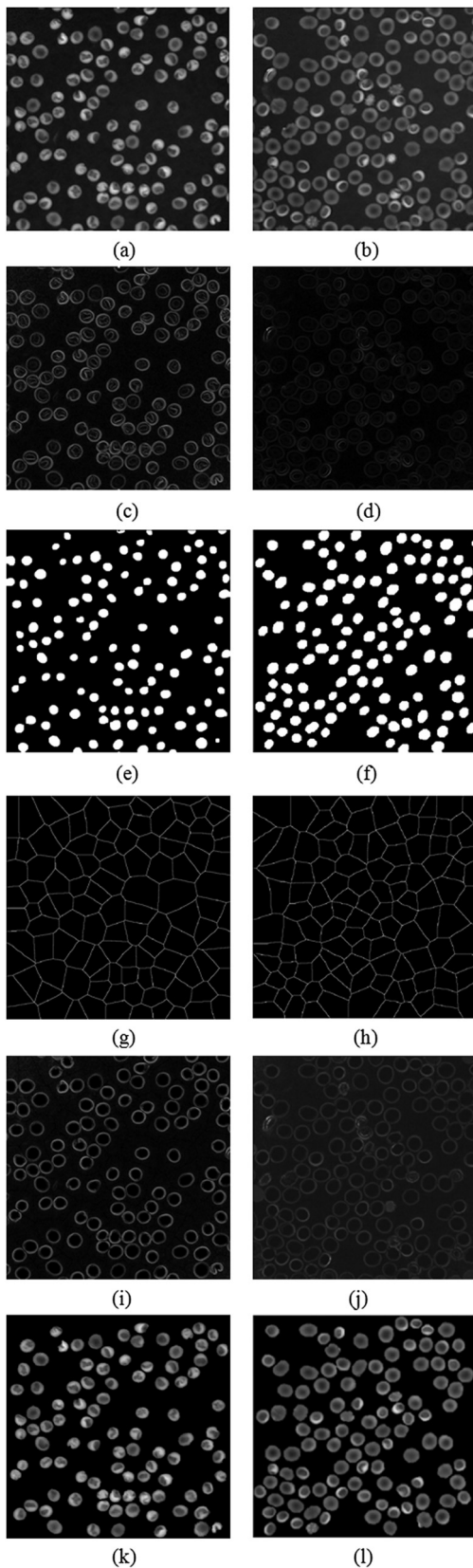


Fig. 9 Key steps of the proposed phase image segmentation. (a) and (b) are the newer and the older RBC QPIs, respectively. (c) and (d) are their corresponding original gradient images, respectively. (e) and (f) are the internal markers, respectively. (g) and (h) are the external markers, respectively. (i) and (j) are the modified gradient images, respectively. (k) and (l) are the segmented QPIs of the newer and the older RBCs, respectively.

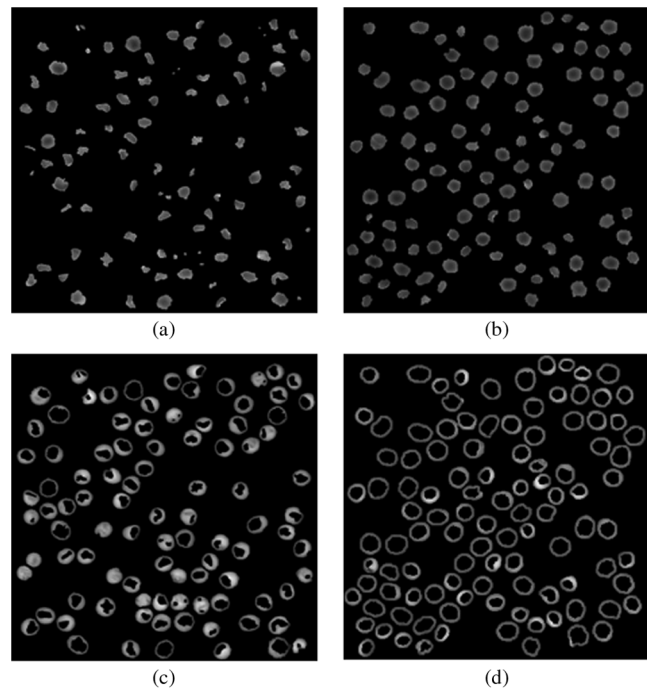


Fig. 10 Segmentation results of the inner and outer parts of the RBC QPI. (a) and (b) are the inner part of the newer and the older RBC QPIs. (c) and (d) are the outer part of the newer and the older RBC QPIs.

background region will be helpful for the analysis of erythrocyte membrane fluctuations.³² Figure 11 shows the statistical distribution of the average phase value of single RBC between two different kinds of RBCs (one with 14 days of storage and the other with 38 days of storage). The average phase value of single RBC is estimated by subtracting the average phase value in the background region of corresponding QPI from the original average phase value within each RBC. As shown in Fig. 11, the mean and standard deviation of RBCs with 14 days storage are 97 deg and 9 deg, respectively. For RBCs with 38 days storage, the mean and standard deviation are 74 deg and 15 deg, respectively. It is noted that there is a difference of approximately 23 deg between the average phase values in the RBCs with the different storage times.

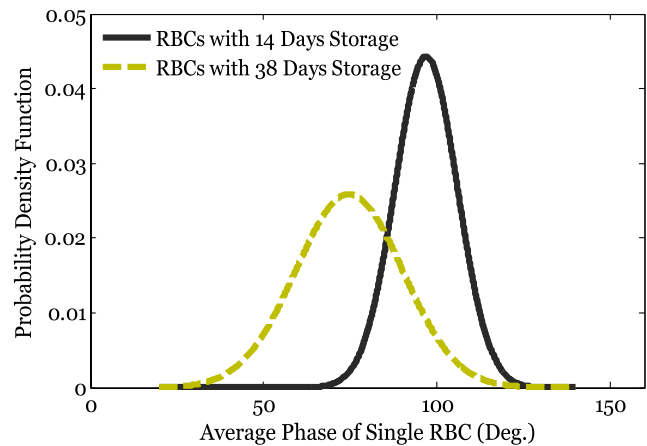


Fig. 11 Distribution of average phase of single RBC after subtracting the average background phase.

6 Conclusion

In this paper, we present a method to successfully segment the quantitative phase images of RBCs for computation of a correct phase value of RBC. Advantages of the proposed method include reducing oversegmentation and undersegmentation. Furthermore, it can obtain the isolated RBC without touching other cells. Our automated RBCs segmentation algorithm enables one to adequately compare the different types of RBCs, since the phase values in the background parts of the RBCs phase image can be set to 0 deg value. After segmentation, we also show that the average background phase for RBCs with different storage time is not the same. Therefore, it is meaningful to segment the RBCs so as to get the correct phase by subtracting the mean of phase corresponding to the background regions. Classification of RBCs traditionally requires a time-consuming manual examination by skilled personnel. We believe that the proposed segmentation algorithm can be helpful for automated classification of RBCs based on RBC characteristics provided by the quantitative phase images generated by digital holographic microscopy.

Acknowledgments

This research was supported by Mid-career Researcher Program through the National Research Foundation of Korea (NRF) funded by the Ministry of Education, Science and Technology (2010-0010391).

References

1. J. Goodman, *Introduction to Fourier Optics*, McGraw-Hill, New York (1996).
2. I. Yamaguchi and T. Zhang, "Phase-shifting digital holography," *Opt. Lett.* **22**(16), 1268–1270 (1997).
3. U. Schnars and W. Jueptner, "Digital recording and numerical reconstruction of holograms," *Meas. Sci. Technol.* **13**(9), R85–R101 (2002).
4. T. Nomura et al., "Phase-shifting digital holography with a phase difference between orthogonal polarizations," *Appl. Opt.* **45**(20), 4873–4877 (2006).
5. Y. Frauel et al., "Three dimensional imaging and display using computational holographic imaging," *Proc. IEEE* **94**(3), 636–654 (2006).
6. P. Ferraro et al., "Controlling image size as a function of distance and wavelength in Fresnel-transform reconstruction of digital holograms," *Opt. Lett.* **29**(8), 854–856 (2004).
7. M. Kim, "Principles and techniques of digital holographic microscopy," *SPIE Rev.* **1**(1), 018005 (2010).
8. P. Marquet et al., "Digital holographic microscopy: a noninvasive contrast imaging technique allowing quantitative visualization of living cells with subwavelength axial accuracy," *Opt. Lett.* **30**(5), 468–470 (2005).
9. M. Antkowiak et al., "Automatic three-dimensional localization of micro-particles using digital holographic microscopy," *Proc. SPIE* **7064**, 7064K1 (2008).
10. L. Martinez and B. Javidi, "Synthetic aperture single-exposure on-axis digital holography," *Opt. Express* **16**(1), 161–169 (2008).
11. B. Javidi et al., "Three-dimensional imaging and recognition of micro-organism using single-exposure on-line (SEOL) digital holography," *Opt. Express* **13**(12), 4492–4506 (2005).
12. F. Dubois et al., "Digital holographic microscopy for the three-dimensional dynamic analysis of *in vitro* cancer cell migration," *J. Biomed. Opt.* **11**(5), 054032 (2006).
13. B. Rappaz et al., "Noninvasive characterization of the fission yeast cell cycle by monitoring dry mass with digital holographic microscopy," *J. Biomed. Opt.* **14**(3), 034049 (2009).
14. I. Moon and B. Javidi, "Volumetric 3D recognition of biological micro-organisms using multivariate statistical method and digital holography," *J. Biomed. Opt.* **11**(6), 064004 (2006).
15. I. Moon et al., "Automated three-dimensional identification and tracking of micro/nanobiological organisms by computational holographic microscopy," *Proc. IEEE* **97**(6), 990–1010 (2009).
16. M. Daneshpanah and B. Javidi, "Segmentation of 3D holographic images using bivariate jointly distributed region snake," *Opt. Express* **14**(12), 5143–5153 (2006).
17. B. Rappaz et al., "Comparative study of human erythrocytes by digital holographic microscopy, confocal microscopy and impedance volume analyzer," *Cytometry Part A*. **73**(10), 895–903 (2008).
18. C. Chesnaud, V. Page, and P. Refregier, "Improvement in robustness of the statistically independent region snake-based segmentation method of target-shape tracking," *Opt. Lett.* **23**(7), 488–490 (1998).
19. R. C. Gonzalez and R. E. Woods, *Digital Imaging Processing*, Prentice Hall, New York (2002).
20. I. Moon et al., "Automated statistical quantification of three-dimensional morphology and mean corpuscular hemoglobin of multiple red blood cells," *Opt. Express* **20**(9), 10295–10309 (2012).
21. E. Cuche, P. Marquet, and C. Depeursinge, "Simultaneous amplitude and quantitative phase contrast microscopy by numerical reconstruction of Fresnel off-axis holograms," *Appl. Opt.* **38**(34), 6994–7001 (1999).
22. T. Colomb et al., "Automatic procedure for aberration compensation in digital holographic microscopy and application to specimen shape compensation," *Appl. Opt.* **45**(5), 851–863 (2006).
23. P. Soille, *Morphological Image Analysis: Principles and Application*, 2nd ed., Springer-Verlag, New York (2003).
24. X. Yang, H. Li, and X. Zhou, "Nuclei segmentation using marker-controlled watershed, tracking using mean-shift, and Kalman filter in time-lapse microscopy," *IEEE Trans. Circuits Syst.* **53**(11), 2405–2414 (2006).
25. F. Meyer, "Topographic distance and watershed lines," *Signal Process.* **38**(1), 113–125 (1994).
26. N. Otsu, "A threshold selection method from gray-level histograms," *IEEE Trans. Syst. Man Cybern. SMC* **9**(1), 62–66 (1979).
27. C. Sun and X. Wang, "Spot segmentation and verification based on improve marker controlled watershed transform," in *3rd International Conf. ICCSIT*, Chengdu, China, Vol. 8, pp. 63–66 (2010).
28. F. A. Sadjadi, "Experimental design methodology: the scientific tool for performance evaluation," *Proc. SPIE* **1310**, 100–107 (1990).
29. W. Press et al., *Numerical Recipes in Fortran 77*, Cambridge University Press, Cambridge (1992).
30. A. Rencher, *Methods of Multivariate Analysis*, Wiley-Interscience, New York (2002).
31. C. G. Koch et al., "Duration of red-cell storage and complications after cardiac surgery," *N. Eng. J. Med.* **358**(12), 1229–1239 (2008).
32. D. Boss et al., "Spatially-resolved eigenmode decomposition of red blood cells membrane fluctuations questions the role of ATP in flickering," *PLoS ONE* **7**(8), 1–10 (2012).